



Efficient design of helical higher-order topological insulators in 3D elastic medium

Jiachen Luo¹, Zongliang Du^{1,2,*}, Hui Chen³, Xianggui Ding¹, Chang Liu^{1,2}, Weisheng Zhang^{1,2}, Xu Guo^{1,2,*}

¹ State Key Laboratory of Structural Analysis, Optimization and CAE Software for Industrial Equipment, Department of Engineering Mechanics, Dalian University of Technology, Dalian, 116023, China

² Ningbo Institute of Dalian University of Technology, Ningbo, 315016, China

³ Piezoelectric Device Laboratory, School of Mechanical Engineering and Mechanics, Ningbo University, Ningbo 315211, China



ARTICLE INFO

Keywords:

Topological materials

Mechanical higher-order topological insulators

Topology optimization

Symmetry indicators

ABSTRACT

Topological materials (TMs) are well-known for their topological protected properties. Phononic system has the advantage of direct observation and engineering of topological phenomena on the macroscopic scale. For the inverse design of 3D TMs in continuum medium, however, it would be extremely difficult to classify the topological properties, tackle the computational complexity, and search solutions in an infinite parameter space. This work proposed a systematic design framework for the 3D mechanical higher-order topological insulators (HOTIs) by combining the symmetry indicators (SI) method and the moving morphable components (MMC) method. The 3D unit cells are described by the MMC method with only tens of design variables. By evaluating the inherent singularity properties in the 3D mechanical system, the classic formulas of topological invariants are modified accordingly for elastic waves. Then a mathematical formulation is proposed for designing the helical multipole topological insulators (MTIs) featured corner states and helical energy fluxes, by constraining the corresponding topological invariants and maximizing the width of band gap. Both valley-based and spin-based mechanical helical HOTIs are obtained by this method and verified by full wave simulations. This design paradigm can be further extended to design 3D TMs among different symmetry classes and space groups, and different physical systems.

1. Introduction

Metamaterials are well-known for its novel modulation of photons, phonons, and matter waves in various applications. Enriching with the topological characteristics, it gives out a new innovative material—topological materials (TMs), which is robust to various defects (Hasan and Kane, 2010, Lu et al., 2014, Xie et al., 2021). Recently, the photonic and phononic TMs have attracted a great research interest in engineering topological phenomena on the macroscopic scale (Lu et al., 2014, Xie et al., 2021, Xu et al., 2022, Christensen et al., 2022, Ma and Shvets, 2016, Wu et al., 2020, Süsstrunk and Huber, 2015, Wu and Hu, 2015, Košata and Zilberberg, 2021, Peano et al., 2021, Long et al., 2018). Related topologically protected states revealed some prospective applications (Lu et al., 2014, Xie et al., 2021, Long et al., 2018, Zhang et al., 2018, Zhang et al., 2018, Nii and Onose, 2023, Kumar et al., 2022, Hafezi et al.,

* Corresponding author.

E-mail addresses: zldu@dlut.edu.cn (Z. Du), guoxu@dlut.edu.cn (X. Guo).

2011, Gong et al., 2020, Bandres et al., 2018, Yu et al., 2018, Ma et al., 2022, Zhou et al., 2020, Zhang et al., 2019).

For example, the quantum spin/valley Hall topological insulators guide the energy flux in a chiral transmission, which alternatively switches the one-way tunnel for the propagated waves with immunity to defects (Ma and Shvets, 2016, Süssstrunk and Huber, 2015, Wu and Hu, 2015, Chen et al., 2019, Xu et al., 2016, Kang et al., 2018, Mousavi et al., 2015, Zhang et al., 2017). That is an ideal way to improve the effectiveness of applications in opto-mechanics, current semiconductor and integrated circuit industry (Zhang et al., 2018, Zhang et al., 2018, Nii and Onose, 2023, Kumar et al., 2022, Hafezi et al., 2011, Gong et al., 2020, Bandres et al., 2018, Yu et al., 2018, Ma et al., 2022, Zhou et al., 2020). For the higher-order topological materials (HOTIs), it is characterized by an intensively localized topological phase within the lower dimensional domain such as the edges and corners (Xie et al., 2021, Wu et al., 2020, Schindler et al., 2019, Benalcazar et al., 2019, Benalcazar et al., 2017). As a pioneering example of the HOTIs, the multipole topological insulators (MTIs) can also provide a multipole moment enhanced topological phases, where the bulk dipole is vanished (Xie et al., 2021, Benalcazar et al., 2019, Benalcazar et al., 2017). Together with the pseudo-spin phenomenon, a helical multipole-induced topological phase is inherited in the helical MTI (Yang et al., 2020, Liu et al., 2019). Those topological phases in the HOTIs are robust to various defects in manufacture, and show a promising prospective in optical/acoustic subwavelength imaging, microelectronics, laser aspects (Xie et al., 2021, Bandres et al., 2018, Zhang et al., 2019, Benalcazar et al., 2017, Zhang et al., 2019, Fan et al., 2019, Kim et al., 2020).

Although the theoretical models have been developed, how to efficiently design 3D unit cells with the demanded topological behaviors is still a crucial challenge. Some typical options include tracing the featured degenerated states near the Dirac points, restricting a special band structure from the band folded mechanism, keeping an obvious Berry curvature (a quantity to topology), or realizing the maximal pseudo-spin energy fluxes in the crossing waveguide (Lu and Park, 2021, Zhu et al., 2018, Chen et al., 2020, Du et al., 2020, Dong et al., 2021, Luo et al., 2021a, Nanthakumar et al., 2019, Christiansen et al., 2019). For instance, unit cells with a Dirac-cone structure are obtained through topology optimization first, then with the help of zone-folding technique, unit cells with double Dirac cone can be generated. By further breaking the symmetry of unit cells manually, spin-Hall insulators are successfully obtained (Nanthakumar et al., 2019). This design process is further enhanced by topology optimization for the symmetry-breaking treatment to obtain unit cells with maximized bandgap width, and more recently, second-order topological insulators have been obtained in a similar way (Chen et al., 2020). Although this design method is quite formal and clear, multiple steps are required and the topological invariant, which is the fundamental character of topological insulators, is not evaluated during the design process. It would be promising to directly obtain topological insulators with prescribed topological invariants through a unified design formulation. To calculate the topological invariants, however, it is very expensive to integrate the Berry curvature or its related terms in the whole Brillouin zone. This issue would be more pronounced for the 3D continuous TMs, which generally cover an infinite design parameter space and are more computationally expensive for analysis and design optimization.

Luckily, the theoretical breakthrough in topological quantum chemistry gives new insight into this bottleneck, from the fruitful meeting between chemistry and physics (in the real and momentum space) (Hoffmann, 1987, Bradlyn et al., 2017, Po et al., 2017, Fu and Kane, 2007). The fundamental tool is calculating the connectivity of band for every real space orbit, with the aids of the elementary band representations (EBRs) or the symmetry indicators (SIs). It gives out the topology in a simple linear function of the symmetry characters at some listed point (Schindler et al., 2019, Benalcazar et al., 2019, Bradlyn et al., 2017, Fu and Kane, 2007). Successful applications of the SI method include the classification of TMs among the whole 230 space and 1651 magnetic groups, and the discovery of thousands of TMs with many uncovered for the first time (Po et al., 2017, Watanabe et al., 2018, Tang et al., 2019). Most recently, the catalogue of topological phononic materials becomes an attractive focus (Xu et al., 2022, Christensen et al., 2022, Peano et al., 2021). This inspires us to efficiently identify the topological properties of the 3D mechanical unit cells using the SI method. It is worth to note that, in the mechanical system, rigid body motions corresponding to zero energy states yield the singularity at some high symmetry point. As a result, the classic formulas derived in the quantum mechanics system need to be modified at first.

Furthermore, how to describe the 3D unit cells is an essential factor for choosing design optimization method (Chen et al., 2020, Dong et al., 2021, Nanthakumar et al., 2019, Christiansen et al., 2019, Bendsøe and Sigmund, 2004). This is because the topological invariants are discrete variables, which cannot in general effectively handled by the gradient-based algorithms. The Moving Morphable Component (MMC) method could describe 3D unit cells using only a few explicit geometry parameters, and this makes it suitable to guarantee a computationally tractable solution process of the inverse design formulation (Guo et al., 2014, Du et al., 2022). In general, we summarize three characteristics of a desired optimization framework of the TMs as: (i) effective to identify the topological characters for arbitrary unit cells; (ii) suitable to topological materials in different classes and different physical systems; (iii) efficient to execute the solution procedure.

In this study, we proposed a unified optimization framework for the 3D continuum TMs by combining the SI method and the MMC method. In this design framework, the helical MTIs with the helical edge and helical corner states can be effectively obtained by simultaneously constraining the modified fractional corner charge and pseudo-spin invariants. The proposed method thoughtfully modified the topological invariants for 3D elastic HOTIs according to the singularity points with zero energy, and successfully obtained optimized 3D helical MTIs in different symmetries, where the in-gap corner states are derived from the quadrupole moment. The numerical simulations of the transmission spectra and crossing waveguide applications validated the intensive corner energy and the chiral energy flux.

The rest of the paper is organized as follows: in Section 2, the governing equations for elastic waves are introduced. And then based on the description method of 3D elastic unit cells using the MMC method and the specialized formulas of topological invariants in Sections 3 and 4, Section 5 proposes an efficient design paradigm for the mechanical helical MTIs. Optimized designs with different symmetries are presented in Section 6 together with the applications in a novel crossing elastic waveguide. Finally, some concluding remarks are discussed in Section 7.

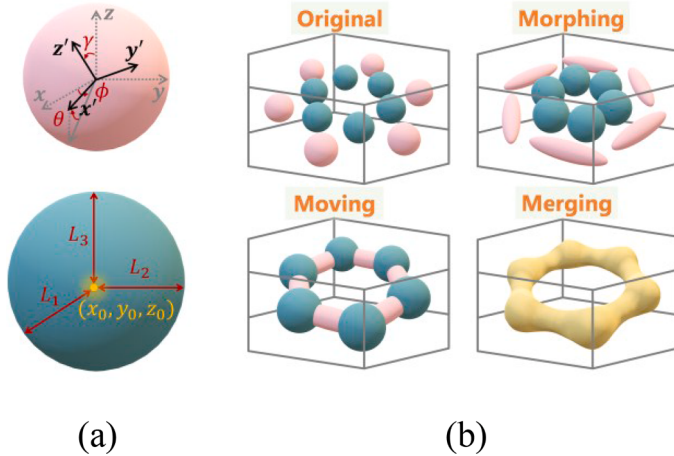


Fig. 1. An illustration of a 3D unit cell described by the MMC method. (a) The geometric description of the 3D components and (b) some representative configurations in the optimization process.

2. The governing equations for elastic waves

In 3D elastic mechanics, the harmonic wave formulation is expressed as (Achenbach, 1973)

$$(\lambda + \mu) \nabla (\nabla \cdot \mathbf{u}) + \mu \nabla^2 \mathbf{u} = -\omega^2 \rho \mathbf{u} \quad (1)$$

where ω is the angular frequency, λ , μ , and ρ are the Lame's parameters and mass density, and $\mathbf{u} = (u, v, w)^\top$ denotes the displacement field.

Since the considered phononic crystal is periodic, the displacement field satisfies the translation condition as $\mathbf{u}(\mathbf{r} + \mathbf{R}) = \mathbf{u}(\mathbf{r})$ with \mathbf{R} denoting the primitive lattice vector. According to the Bloch theorem, the harmonic elastic wave propagation can be determined by the following discretized equations

$$\mathbf{K}\mathbf{U} = -\omega^2 \mathbf{M}\mathbf{U} \quad (2)$$

$$\mathbf{U}(\mathbf{r}_0 + \mathbf{R})|_{BC} = \mathbf{U}(\mathbf{r}_0)|_{BC} e^{i\mathbf{k}\cdot\mathbf{R}}$$

Here, the matrices \mathbf{K} and \mathbf{M} refer to the stiffness and mass matrixes, and \mathbf{U} is the eigenvector.

In order to handle the periodic constraints in the above eigenvalue problem, the standard Lagrange multiplier method is adopted (Strang, 1993). By defining a Lagrange multiplier Λ , Eq. (2) can be reformulated as

$$\begin{bmatrix} \mathbf{K} + \omega^2 \mathbf{M} & \mathbf{N}_f \\ \mathbf{N} & \mathbf{0} \end{bmatrix} \begin{bmatrix} \mathbf{U} \\ \Lambda \end{bmatrix} = \mathbf{0} \quad (3)$$

in which the constraint matrixes \mathbf{N} and \mathbf{N}_f are used to homogenize the eigenvalue problem.

Now, let us decompose the eigenvector with the solution \mathbf{U}_c as $\mathbf{U} = \mathbf{N}_{null}\mathbf{U}_c + \mathbf{U}_0$, where the matrix \mathbf{N}_{null} and vector \mathbf{U}_0 belong to the null space of \mathbf{N} . An allowable value is $\mathbf{U}_0 = \mathbf{0}$. After left multiplying Eq. (3) by \mathbf{N}_{null}^\top (\mathbf{N}_{null} is the null space of \mathbf{N}_f^\top), we have the final governing equation of the 3D elastic wave as

$$\mathbf{K}_c \mathbf{U}_c = -\omega^2 \mathbf{M}_c \mathbf{U}_c \quad (4)$$

where the eliminated stiffness matrix is $\mathbf{K}_c = \mathbf{N}_{null}^\top \mathbf{K} \mathbf{N}_{null}$, and the eliminated mass matrix is $\mathbf{M}_c = \mathbf{N}_{null}^\top \mathbf{M} \mathbf{N}_{null}$. Since Eq. (3) requires $\mathbf{N}_f \Lambda = \mathbf{0}$, it is needless to solve for it since Λ is useless, and a practical choice is setting $\mathbf{N}_f = \mathbf{N}^\top$, then $\mathbf{N}_{null} = \mathbf{N}_{null}$.

Besides the topology optimization with finite element analysis method, we also note that other numerical analysis method (such as IGA) can be incorporated with topology optimization for the rational design of advanced structures (Ghasemi et al., 2018). By taking the advantages of IGA, such design method would be more beneficial for physical problems governed by higher-order partial differential equations, e.g., flexoelectricity (Ghasemi et al., 2018).

3. Description of the 3D unit cells via the MMC method

Structural topology optimization has been successfully applied to inverse design various topological metamaterials (Peano et al., 2021, Zhu et al., 2018, Chen et al., 2020, Du et al., 2020, Dong et al., 2021, Luo et al., 2021a, Nanthakumar et al., 2019, Christiansen et al., 2019, Luo et al., 2021b). For designing the 3D elastic topological materials, we adopt the Moving Morphable Component (MMC) method (Du et al., 2020, Luo et al., 2021a, Guo et al., 2014, Du et al., 2022, Luo et al., 2021b), which has the advantages of the explicit geometry description and improved computational efficiency.

The building block in the MMC method is a set of morphable components, described by some geometry parameters, such as the center coordinate, length, width, and thickness. As a result, through updating those geometry parameters, every component can move, morph, merge or disappear to form the optimized structure, as shown in Fig. 1. In this way, the optimal parameter space will be deeply shrunk, and the solution efficiency will be significantly improved.

In our work, each 3D component (the inclusion phase) is explicitly characterized by the ellipsoid with a design variable vector $\mathbf{D}_i = (\mathbf{r}_{0i}^\top, \mathbf{L}_i^\top, \boldsymbol{\Phi}_i^\top)^\top$, i.e., the center coordinate $\mathbf{r}_0 = (x_0, y_0, z_0)^\top$, the length of semi-axes $\mathbf{L} = (L_1, L_2, L_3)^\top$, and the Euler rotation angles $\boldsymbol{\Phi} = (\theta, \phi, \gamma)^\top$, as shown in Fig. 1(a). In this manner, each MMC can be explicitly determined by only 9 design variables. Furthermore, in a unit cell, the inclusion phase is identified by the topology description function $g_i(\mathbf{r}, \mathbf{D}_i)$ for each component expressed with its covered region Ω_i as

$$g_i(\mathbf{r}, \mathbf{D}_i) \equiv \|\mathbf{r}'\|^2 - 1 = \begin{cases} > 0 & \text{if } \mathbf{r} \in \Omega_i \\ = 0 & \text{if } \mathbf{r} \in \partial\Omega_i \\ < 0 & \text{else} \end{cases} \quad (5)$$

In Eq. (5), the local coordinates \mathbf{r}' are determined by the global coordinates \mathbf{r} and the rotation matrix $\mathbf{R}(\boldsymbol{\Phi})$ as

$$\mathbf{r}'_i = \frac{1}{L_i} \mathbf{R}_{ij}(\boldsymbol{\Phi}) (\mathbf{r}_j - \mathbf{r}_{0j}) \quad (6)$$

According to the symmetry requirement of the unit cells, only the MMCs in a reduced design domain need to be optimized and they can be transformed to the rest part. Furthermore, all the inclusions represented by MMCs in the design domain can be smoothed by the K-S aggregation technique (Kreisselmeier and Steinhauser, 1980) or the Boolean operation (adopted by this work).

4. The SI induced topological invariants of the helical MTIs

The helical multipole topological insulators (helical MTIs) (Yang et al., 2020, Liu et al., 2019), as a compound topological material, should simultaneously hold the characters (or the topological invariants) from the multipole moment and the pseudo-spin. In general, the calculation of topological invariants is computationally expensive for the continuum unit cells. Nevertheless, recent work in topological quantum chemistry reveals a rapid approach to identify topological invariants through its symmetry indicators (SIs) (Xu et al., 2022, Watanabe et al., 2018, Tang et al., 2019, Po et al., 2017). Next, we will introduce the SI method into the calculation of topological invariants, and then give out the method to design helical MTIs.

Actually, based on the graph theory and group theory, the SI method gives a universal description for the connectivity of band structures (Bradlyn et al., 2017, Po et al., 2017, Bradlyn et al., 2018). This method implies that once the symmetries of states at all high-symmetry points are recognized, we can identify its topology. To change the topology, one can break the symmetry of states at the high-symmetry points. Based on this principle, the SI method gives a strategy to count the symmetric states, and thus presents a judgement whether a material can be adiabatically evolved from a topologically nontrivial phase or not (Xu et al., 2022, Christensen et al., 2022, Bradlyn et al., 2017, Watanabe et al., 2018, Tang et al., 2019, Po et al., 2017).

Based on the SI method, for a spinless $C_{n=3,6}$ -symmetric mechanic system with the time reversal symmetry (TRS), we identify the eigenvalue $\Pi_q^{(n)}$ of the \widehat{C}_n rotational operator as (Benalcazar et al., 2019, Benalcazar et al., 2017, Bradlyn et al., 2017)

$$\langle w(\Pi) | \widehat{C}_n | w(\Pi) \rangle \in \left\{ \Pi_q^{(n)} | \Pi_q^{(n)} = e^{\frac{i2\pi(q-1)}{n}}, q = 1, \dots, n \right\} \quad (7)$$

where $w(\Pi)$ denotes the z -component of the displacement at the high-symmetry point Π . The symbol $\#\Pi_q^{(n)}$ counts the number of states associated with the eigenvalue of $\Pi_q^{(n)}$ below the target band gap. Or, setting the Γ point as a reference, define the SI at Π as $[\Pi_q^{(n)}] = \#\Pi_q^{(n)} - \#\Gamma_q^{(n)}$. At the high-symmetry points, it satisfies $\widehat{C}_n \mathbf{k} = \mathbf{k} + \mathbf{G}$ with \mathbf{G} denoting the reciprocal lattice vector. For the C_3 -symmetric hexagonal unit cells, the high-symmetry points include Γ and K in the C_3 symmetry, while for the C_6 -symmetric hexagonal unit cells, they include Γ in the C_6 symmetry, K in the C_3 symmetry, and M in the C_2 symmetry, respectively. In this manner, the topological classification is determined completely by the corresponding SIs, such as the fractional corner charge and the pseudo-spin invariants in the following contents.

4.1. The fractional corner charge invariants

For the MTIs, the fractional corner charge $Q^{(n)}$ is an effective topological invariant to determine the multipole moment and the topological corner states (Schindler et al., 2019, Benalcazar et al., 2019, Benalcazar et al., 2017). For the $C_{n=3,6}$ -symmetric mechanical topological system, we propose the following formulas (Benalcazar et al., 2019, Benalcazar et al., 2017, Bradlyn et al., 2017)

$$\begin{aligned} Q^{(3)} &= \left(\frac{1}{3} \left(\#K_{q \neq 1}^{(3)} - \frac{1}{2} \#\Gamma^{(3)} \right) \bmod 1 \right) \times ((\#\Gamma^{(3)} + 1) \bmod 2) \\ Q^{(6)} &= \left(\frac{1}{4} [M_1^{(2)}] + \frac{1}{6} [K_1^{(3)}] \right) \bmod 1 \end{aligned} \quad (8)$$

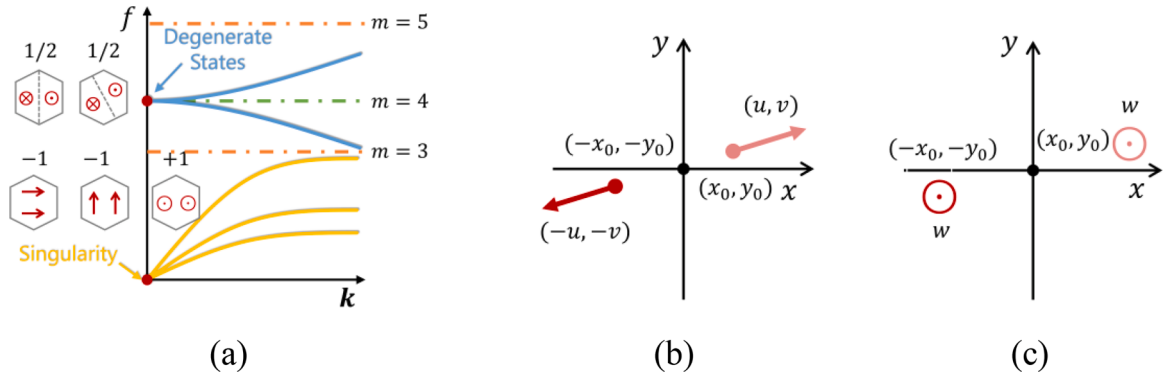


Fig. 2. The script of the modification procedure. (a) The singularity in mechanics and degenerate states in a hexagonal unit cell. (b) and (c) The vector transformation of displacement component (u, v) and w . Here, only the degenerate states are calculated under the \hat{C}_3 operator, and the corresponding eigenvalue of the degenerate states is $1/2 = (e^{i2\pi/3} + e^{i4\pi/3})/2$ (as the superposition of the eigenvalues of the \hat{C}_3 operator); the other states are calculated under the \hat{C}_2 operator.

Here, the red terms in the function of $Q^{(3)}$ are introduced to avoid the confused distinction of the unpaired degenerate states (Ma and Shvets, 2016, Wu and Hu, 2015, Košata and Zilberberg, 2021, Xu et al., 2016). As an alternative strategy, $\#\Gamma^{(3)}$ counts the two-order degeneracy at the Γ point, and $\#\Gamma^{(3)}/2$ identically equals the $\#\Gamma_2^{(3)}$ or $\#\Gamma_3^{(3)}$. The red modulo term in $Q^{(3)}$ guarantees the degenerate states to be in pairs (i.e., $\#\Gamma^{(3)}$ is an even number). For a visualization, the Fig. 2 shows that our modification successfully corrected the confused distinction of degenerate states when $m = 4$. For more details, refer to Appendix A.

4.2. The pseudo-spin invariants

For the photonic/phononic quantum spin/vortex Hall effects, the protected chiral energy flux can be well identified from the pseudo-spin vortex phenomenon. So, an alternative approach is adopted through tracing the (broken) Dirac cone and band inversion (Wu and Hu, 2015, Košata and Zilberberg, 2021, Xu et al., 2016, Zhu et al., 2018, Du et al., 2020, Luo et al., 2021a, Nanthakumar et al., 2019, Christiansen et al., 2019). Practically, for the 3D C_3 - and C_6 -symmetric unit cells, the pseudo-spin invariants are modified as (Košata and Zilberberg, 2021, Schindler et al., 2019)

$$\begin{aligned} Z^{(3)} &= \text{sgn}\left(\#\Gamma_2^{(3)} - \#\Gamma_3^{(3)}\right) \\ Z^{(6)} &= \text{sgn}\left(\#\Gamma_p^{(6)} - \#\Gamma_d^{(6)} - 2\right) \end{aligned} \quad (9)$$

Here, terms $\#\Gamma_p^{(6)}$ and $\#\Gamma_d^{(6)}$ count the state p and state d under the \hat{C}_6 operator for the Γ point, respectively. Notably, the subtracted red term is introduced to correct the $\#\Gamma_p^{(6)}$ due to the singularity in the 3D elastic wave (the singularity is marked as the state p) (Christensen et al., 2022, Watanabe and Lu, 2018). For the 3D elastic wave, the singularity relates to three translational motions, their displacement and vector transformation are shown in Fig. 2. This vector transformation implies two independent symmetries of component (u, v) and w , and that's reason why we only used the z -component in Eq. (7). This modification is based on counting all occupied bands below the target band gap, including the first three bands crossed through the singularity. Furthermore, the counting idea keeps target bands isolated from other bands, as the SI method requires. For more details, refer to Appendix B.

5. An efficient design paradigm of 3D mechanical helical MTIs

With the above topological invariants presented in Eqs. (8) and (9), we can now design the helical MTIs using explicit topology optimization method. The corresponding optimization formulation and solution process are introduced as follows.

5.1. Mathematical formulation

Combining the MMC-based description method and the modified formulas of topological invariants in elastic medium, optimized 3D helical MTIs can be obtained by solving the following mathematical formulation:

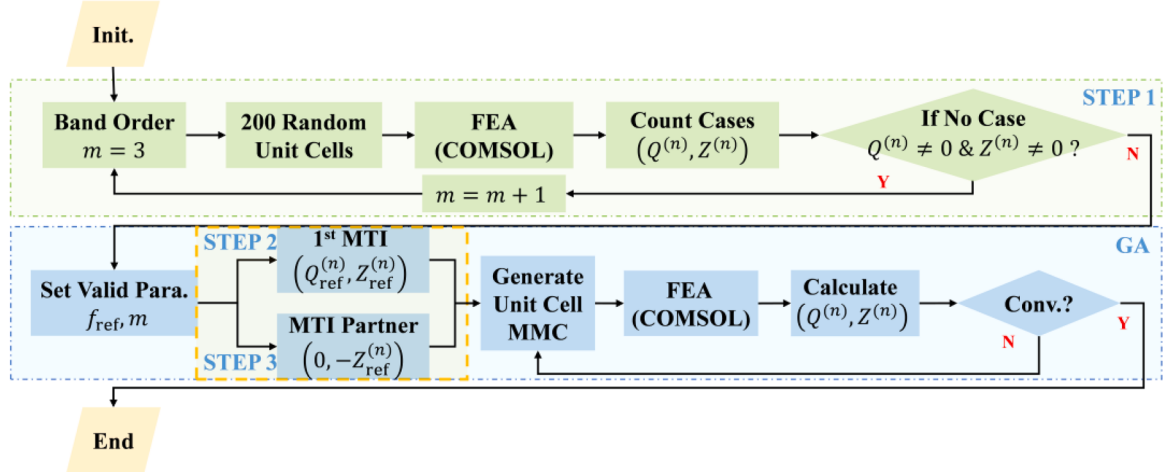


Fig. 3. The scheme of optimization for the helical MTIs.

$$\begin{aligned}
 \text{find} \quad & \mathbf{D} = (\mathbf{D}_1^\top, \dots, \mathbf{D}_N^\top, H)^\top \\
 \text{max} \quad & \min(f_{\text{ref}} - \max_k f_k^m, \min_k f_k^{m+1} - f_{\text{ref}}) \\
 \text{s.t.} \quad & \mathbf{K}_c \mathbf{U}_c = -\omega^2 \mathbf{M}_c \mathbf{U}_c \\
 & (\mathbf{Q}^{(n)}, \mathbf{Z}^{(n)}) = (\mathbf{Q}_{\text{ref}}^{(n)}, \mathbf{Z}_{\text{ref}}^{(n)}) \\
 & \mathbf{D}_{\min} \leq \mathbf{D} \leq \mathbf{D}_{\max}
 \end{aligned} \tag{10}$$

In the design variable vector, \mathbf{D}_i describes the i th component in the slab with a thickness H (in the z -axis), as illustrated in Fig. 1. By denoting the eigenfrequency of the m th band as f^m , the gap width between the m th and $(m+1)$ th bands is maximized with a target mid-frequency f_{ref} . The third equation in Eq. (10) is the governing equation for the 3D elastic waves. Since the fractional corner charge and the pseudo-spin invariants simultaneously contribute to the existence of helical corner states, the target topology invariants $(\mathbf{Q}_{\text{ref}}^{(n)}, \mathbf{Z}_{\text{ref}}^{(n)})$ is introduced as a constraint. The last inequality persists the lower and upper bounds of the design variable vector.

In principle, by updating the governing equation and target topological invariants, the mathematical formulation in Eq. (10) can be applied for designing TMs among different symmetry classes, and different physical systems. In this work, we focused on the inverse design of 3D helical MTIs in elastic medium with C_3 and C_6 symmetries.

5.2. Solution process

Since the topological invariants are quantized, gradient-based optimization algorithms would be ineffective for solving Eq. (10). Thanks to the advantage of a fewer number of design variables in the MMC method, the genetic algorithm (GA) is adopted here and the settings are presented in Appendix C. To be specific, the flowchart for the rational design of helical MTIs is shown in Fig. 3, and its solution process is summarized as follows:

- STEP 1: Initialization of the MMC method and the GA solver.

The gap label m , the mid-frequency f_{ref} , and the nonzero topological invariants $(\mathbf{Q}_{\text{ref}}^{(n)}, \mathbf{Z}_{\text{ref}}^{(n)})$ are initialized first through a trial process, starting from $m = 3$;

- STEP 2: Optimal design of the first MTI.

With the parameters determined in STEP 1, solve the mathematical programming Eq. (10) to obtain the first optimized MTI with the predefined invariant $(\mathbf{Q}_{\text{ref}}^{(n)}, \mathbf{Z}_{\text{ref}}^{(n)})$ and mid-frequency f_{ref} ;

- STEP 3: Optimal design of the MTI partner (if necessary).

With the desired topological invariants setting as $(0, -Z_{\text{ref}}^{(n)})$ and the other parameters the same as STEP 2, solve Eq. (10) to obtain the optimized MTI partner who has the inverted pseudo-spin effect.

To illustrate the effectiveness of the proposed design framework, the statistical charts of the states at the Γ point (6000 samples) and of different TMs (8000 samples) are illustrated in Fig. 4(a) and 4(b), respectively. It can be found that, using Eq. (8), the states \mathbf{p} and

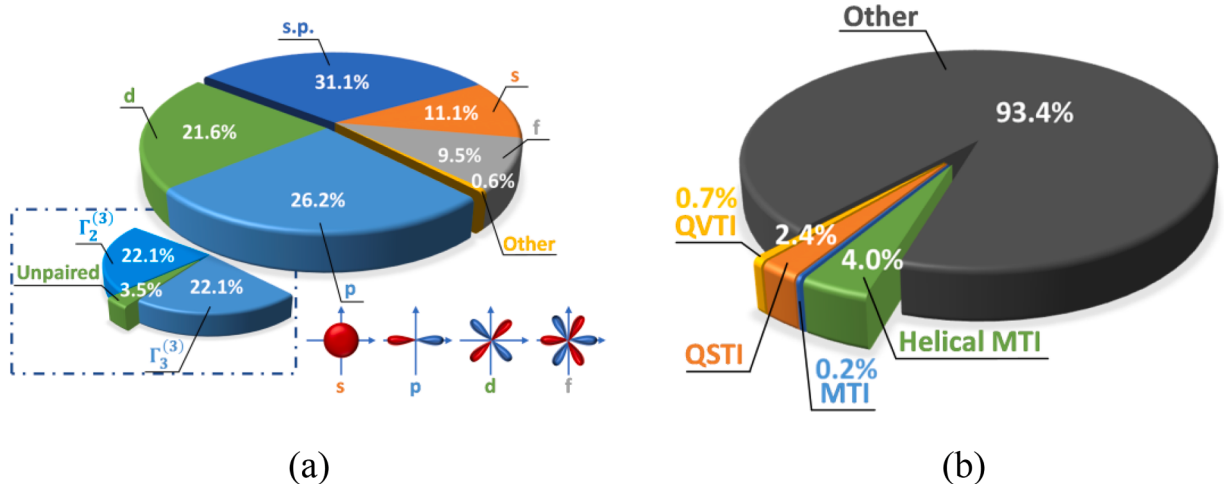


Fig. 4. The statistical charts (a) of different states at the Γ point (the partitions of p and d would be decomposed into the boxed partitions without the modification in Eq. (8)), (b) of different TMs. Hint: s.p. refers to the singularity point, and the inserted right-below diagrams in (a) show the profiles of s-, p-, d- and f-states.

d are successfully identified, and they take about 21.6% and 26.2% of the whole set as shown in Fig. 4(a). Without the modification in Eq. (8), however, such states would be decomposed to $\Gamma_2^{(3)}$ state (22.1%), $\Gamma_3^{(3)}$ state (22.1%), and an unpaired set of state (3.5%). This unpaired set would further make troubles for the calculation of the fractional corner charge invariant. In Fig. 4(b), 6.6% of samples are four typical TMs (quantum spin/valley Hall topological insulators (QSTIs/QVTIs), MTIs and helical MTIs), while the desired helical MTIs only account for 4.0%. This validates the necessity of developing an inverse design paradigm for the helical MTIs. More discussions about the setting of components and materials in the optimization framework is presented in Appendix E and Appendix F.

6. Applications of the MMC-based design framework for 3D helical MTIs in elastic medium

In the present work, the helical MTIs are periodic in the in-plane direction and made of the basic medium EP and scattering medium Fe (materials parameters and more setup details are referred to Appendix C).

6.1. Optimal design of valley-based mechanical helical MTIs

Under the optimization framework, the optimized C_3 -symmetric valley-based helical MTIs are obtained in Fig. 5(a). And there is a normalized bulk band gap at 0.741–1.069 between the 6th and 7th bands (colored in grey in Fig. 5(a)). The symmetry behaviors of the high-symmetry points are shown in the Fig. 5(c). There are three broken degenerate states (from the Dirac cone) at the K point below the target bandgap, while only the third one is unpaired and implies the possibility of a phase vortex. The phase field of this unpaired state is also inserted in Fig. 5(b). The fractional corner charge and the pseudo-spin invariants are (2/3, 1).

In order to realize the band inversion, the corresponding MTI partner can be easily constructed by applying the spatial reversal operation, or in other words, its invariants are (0, -1). An opposite pair of $Z^{(3)}$ invariants would produce a helical topological state from the bulk-boundary correspondence. Moreover, a pair of zero and nonzero fractional corner charges reveal the appearance of corner states (Gong et al., 2020), as shown in Fig. 6(a) around the normalized frequencies of 0.897 and 0.966. The latter localized corner state is displayed in the inserted diagram.

Besides, the full-wave transmission is presented in Fig. 6(b), where energy is captured from different regions around the outer bulk, the interface edges, and the interface corners. A clockwise helical source is excited near the supercell's center, shown as the star in Fig. 6(c). The transmission reveals some edge energy peaks are around the normalized frequencies of 0.793 and 1.001, and some intensively localized corner states are around the normalized frequencies of 0.897 and 0.966. For a clear visualization, the corresponding bulk, edge, and corner energy fields are displayed in Fig. 6(c). In contrast to the edge gap around the normalized frequency range of 0.872–1.001 (colored in light-green), those in-gap corner states are derived from the multipole moment.

For the verification of the helical behavior, a biased helical source off the center is excited additionally, as shown in Fig. 6(d). It illustrates the edge state appears at 0.862, and is outside the edge gap of 0.872–1.001, to show the energy flux more clearly. The inserted arrow diagrams displayed the energy flux near their corners and edges. We found that these two supercells had significant opposite responses under different exciting helical sources (clockwise or anticlockwise). All their corners held a clear energy vortex. Their edge energy fluxes are locked by their exciting sources and only could flow forward or backward.

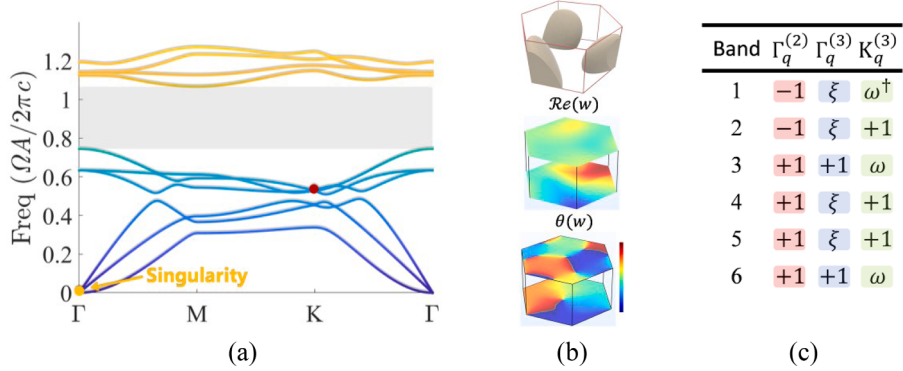


Fig. 5. The optimized valley-based mechanical helical MTIs. (a) The band structure, (b) the unit cell, the $\mathcal{R}e(w)$ and $\theta(w)$ fields of the unpaired state. (c) The symmetry-behavior-table, in which the degenerate states are tagged as $\omega = e^{i2\pi/3}$ for the K point, while for the Γ point they are tagged as ξ . Their states are visualized in the Appendix C.

6.2. Optimal design of spin-based mechanical helical MTIs

For the optimized C_6 -symmetric spin-based helical MTI pairs, as illustrated by the band structures shown in Fig. 7(a) and (e), band gaps are observed in the normalized frequency ranges of 1.344–1.489 and 1.332–1.450 respectively. Below the gap, there are four degenerate states found at the Γ points for both cases, but only the last two states formed an unpaired double Dirac cone, which features the pseudo-spin vortex. The displacement fields of these unpaired states are inserted in Fig. 7(b) and (f), from which the band inversion is clearly displayed. The symmetry behaviors in Fig. 7(c) and (g) show that the fractional corner charges and the modified pseudo-spin

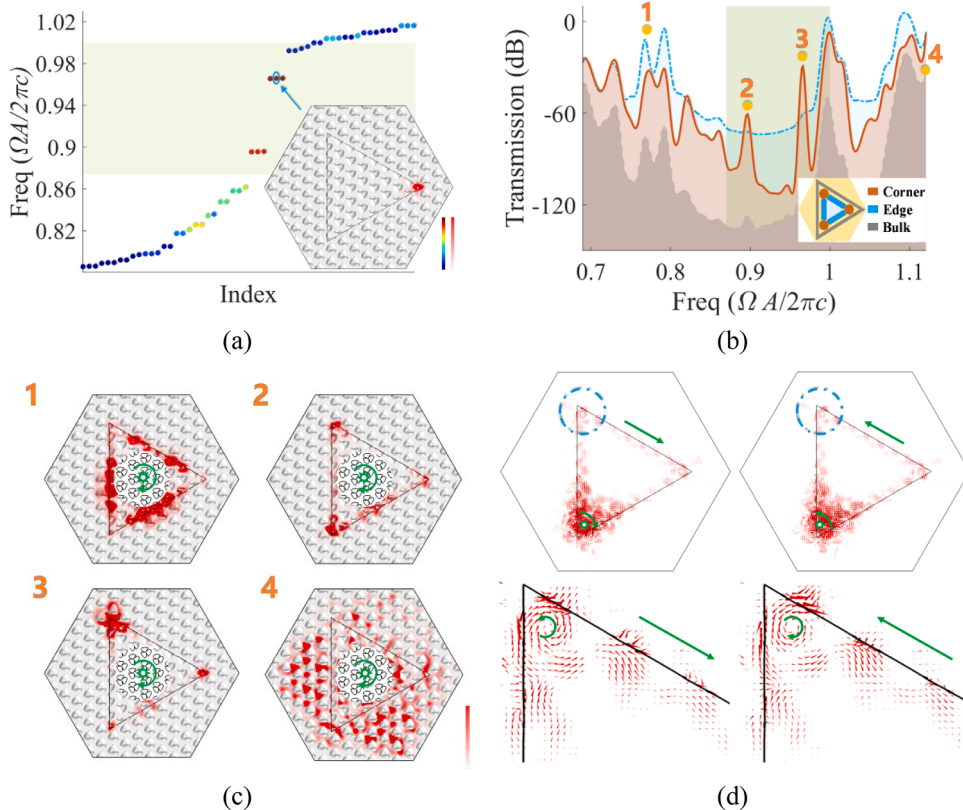


Fig. 6. Simulation results of the optimized valley-based helical MTIs. (a) The eigenvalue spectrum (points are colored according to the corner energy intensity) and the energy field of a corner state. (b) The transmission spectra from the probes in bulk, edge, and corner area (colored in legend). (c) Energy fields tagged in (b) with the normalized frequencies of 0.793, 0.897, 0.966, and 1.121, respectively. (d) The energy flux and their zoom-in views of helical edge states at the normalized frequency of 0.862.

invariants are $(1/2, 1)$ and $(0, -1)$, respectively. Specifically, the pair of opposite $Z^{(6)}$ invariants lock the energy flux by the pseudo-spin phenomenon. In contrast, the pair of zero and nonzero fractional corner charges predict the topological corner states (according to the vanished bulk polarization in C_6 -symmetric unit cells, these nonzero corner fractional charges are only derived from the multipole moment (Benalcazar et al., 2019)). By combining these two topological characters, the topological corner state will also have pseudo-spin behaviors and present as a helical corner state. For a verification of this helical corner state, the eigenvalue spectrum and the pseudo-spin energy flux of the supercell's simulations are shown in Fig. 7(d) and (h), and its energy density distribution is highly localized at corners at the normalized frequency of 1.426.

6.3. Applications of the optimized helical MTIs in a crossing waveguide

As an application of the helical MTIs, a crossing waveguide (a single layer) composed of the two optimized C_3 -symmetric helical MTIs in Subsection 6.1 (colored blue/yellow for the original/inversed TMIs mentioned above) is developed in Fig. 8(a). Since the additional pseudo-spin freedom locks the energy flux in the waveguide, two opposite transmissions would be discovered when we sequentially excited the Port 1 and Port 2. By gradually modulating the exciting frequency, the energy will spread through the center wall and induce the output corner states.

The simulations in the normalized frequency range of 0.7-1.1 are processed to test the performance of the waveguide, as shown in Fig. 8(b). It is clear that when Port 1 is excited at the normalized frequency of 0.776, the energy only transmits to Port 2 and Port 3, yet it only transmits to Port 1 and Port 4 from Port 2. This phenomenon reveals the locked helical energy flux as expected. At the normalized frequency of 0.897, the corner states in the lower half of the waveguide are excited in both cases. Here, these states stay in the band gap of the edge state (i.e., 0.872-1.001, refer to Appendix D for more details), and their energy only localizes at corners, and no edge states exist.

To test the working range of the one-way transmission in this waveguide, we distinguished the energy from the different ports (Port 3 or Port 4), as shown in Figs. 8(c) and 8(d). Here the light-green area and yellow-solid points refer to the band gap of the edge state and the states in Fig. 8(b). In this much wider frequency range of 0.749-0.861, the average difference between both ports is higher than 10dB. When we reverse the exciting port, the output port, which has a higher transmission, is also turned, as shown in Fig. 8(d). In this frequency range, the first two edge bands, as illustrated in Appendix D, will be excited. Hence, these one-way transmission results from the helical edge states. Moreover, the corner states tagged with the number 2 and number 4 are in the gap of the edge state but display an apparent energy concentration from the exciting source.

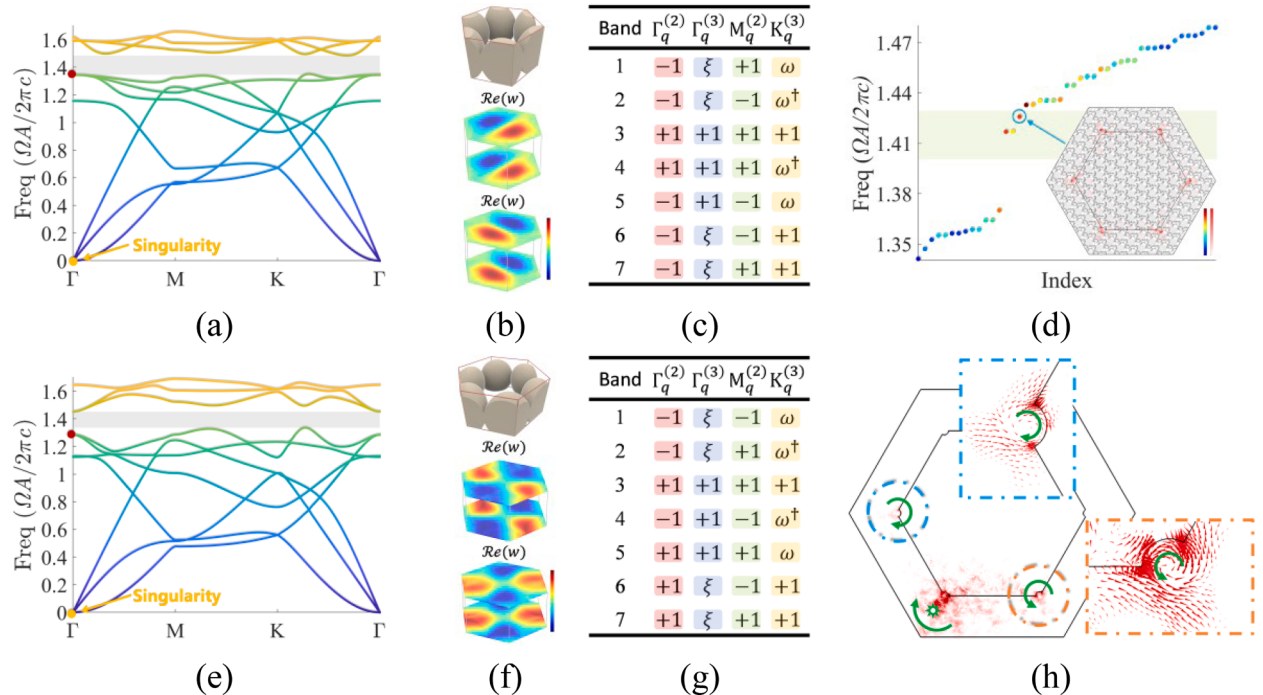


Fig. 7. Simulation results of the optimized spin-based helical MTIs. (a) and (e) The band structures. (b) and (f) The optimized unit cells and the displacement field $\mathcal{R}_e(w)$ of the unpaired states. (c) and (g) The symmetry-behavior-tables. Here, (a)-(c) and (e)-(g) relate to the 1st and 2nd C_6 -symmetric unit cells in Table C1, respectively. Their states are visualized in the Appendix C. (d) The eigenvalue spectrum (points are colored according to the corner energy intensity) and (h) the energy flux of the corner states at the normalized frequency of 1.426.

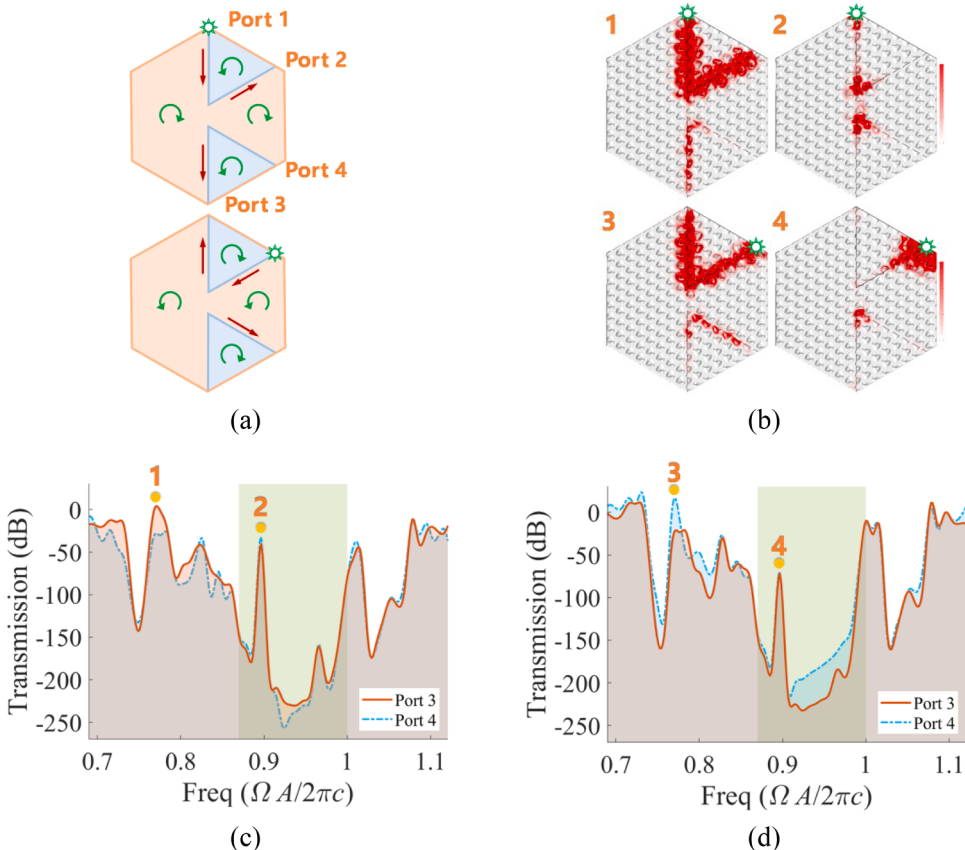


Fig. 8. The crossing waveguide made of the optimized C_3 -symmetric helical MTIs. (a) The sketches of the waveguide and its energy fluxes in different exciting cases (the exciting line sources are tagged as stars). (b) The energy fields at the normalized frequencies of 0.776 and 0.897. The measured transmission of Ports 3 and 4 (c) from the exciting Port 1 or (d) from the exciting Port 2. Here the band gap of the edge state (light-green region) and some typical states (yellow-solid points) are colored.

7. Concluding remarks

In this work, we proposed an optimization framework for the inverse design of multi-functional topological materials in the 3D continuous medium. By carefully manifesting the degenerate states and singularity points in the elastic waves, the 3D helical multipole topological insulators are well-classified by the fractional corner charge and the pseudo-spin invariants. With the explicit topology optimization and the symmetry indicator methods, the proposed design paradigm has the advantages of (1) rapid classification of the 3D topological materials and (2) efficient optimization of the 3D continuum unit cells in a smaller parameter space. This framework shows outstanding suitability to the 3D topological system and can also be generalized to other symmetry classes and space groups. Besides, building up a topological materials library in continuous medium would be an exciting topic for further research.

8. Methods

The solid mechanic simulation is performed in the commercial software COMSOL MULTIPHYSICS. The default open surfaces are set as free boundaries. The Bloch theorem is numerically expressed by the Floquet periodic boundaries. In common, the energy in solid mechanics is consistent in distribution as the square of amplitude in total displacement $\| (u, v, w) \|_2^2$.

Statement of novelty

We proposed a unified optimization framework for the 3D topological materials in the continuum medium. Considering the singularity effect in the 3D mechanical system, the classic formulas about the fractional corner charge invariant and the pseudo-spin invariant are modified. By taking the advantages of the Moving Morphable Components method (MMCs) and the Symmetry Index (SI) method, the mathematical formulation developed for 3D mechanical HOTS significantly saves the computational cost with a shrunk parameter space. Optimized valley-based and spin-based mechanical HOTS with topologically protected corner and edge states, and the helical transmission were obtained. The proposed design paradigm can be generalized to design 3D topological

materials efficiently and rationally among different topological classes, space groups and physical systems.

CRediT authorship contribution statement

Jiachen Luo: Conceptualization, Methodology, Formal analysis, Software, Visualization, Writing – original draft, Writing – review & editing. **Zongliang Du:** Conceptualization, Methodology, Supervision, Formal analysis, Writing – review & editing, Funding acquisition. **Hui Chen:** Methodology, Supervision, Writing – review & editing. **Xianggui Ding:** Software, Visualization, Writing – review & editing. **Chang Liu:** Writing – review & editing. **Weisheng Zhang:** Writing – review & editing. **Xu Guo:** Conceptualization, Methodology, Supervision, Writing – review & editing, Funding acquisition.

Declaration of Competing Interest

There are no conflicts to declare.

Data availability

Data will be made available on request.

Acknowledgements

The financial supports from the National Natural Science Foundation (11821202, 12002073, 12002077, 12272075), Dalian Talent Innovation Program (2020RQ099), the Liaoning Revitalization Talents Program (XLYC2001003, XLYC1907119), the Fundamental Research Funds for the Central Universities (DUT20RC(3)020, DUT21RC(3)076, DUT22QN238), and 111 Project (B14013) are gratefully acknowledged.

Appendix

Appendix A: Modification of the fractional corner charge invariant

With the aid of the SI method, the computational process of topology can be practically simplified. For example, the fractional corner charge in the C_3 -symmetric hexagonal unit cells can be expressed with SI method as (Benalcazar et al., 2019, Benalcazar et al., 2017, Bradlyn et al., 2017)

$$Q_q^{(3)} = \frac{1}{3} \left[K_{q \neq 1}^{(3)} \right] \bmod 1 \quad (\text{A1})$$

where subscript q equals 2 or 3 depending on the setup of the constructed supercell. Moreover, due to the TRS and C_3 symmetry, some

Table A1

The symmetry behaviors of the C_3 -symmetric unit cells with TRS (for the fractional corner charge invariants)

$Q_{q=2}^{(3)}$	$Q_{q=3}^{(3)}$	$\#K_2^{(3)}$	$\#K_3^{(3)}$	$\#\Gamma^{(3)}$	$\#\Gamma_2^{(3)}$	$\#\Gamma_2^{(3)}$
1/3	0	1	0	0	0	0
0	1/3	0	1	0	0	0
0	2/3	1	0	2	1	1
0	0	1	1	2	1	1
0	0	1	0	1	1	0
0	0	0	1	1	0	1
0	0	1	0	1	0	1
0	0	0	1	1	1	0

two-order degenerate states are protected at the Γ point, such as the states with eigenvalue $\Gamma_2^{(3)}$ and $\Gamma_3^{(3)}$. Those degenerate states will make some linear combinations, and they are computationally expensive to identify clearly, especially for the unpaired degenerate states (Ma and Shvets, 2016, Wu and Hu, 2015, Košata and Zilberberg, 2021, Xu et al., 2016, Zhang et al., 2017). Instead, we termed the invariant with the number of the two-order degenerate states $\#\Gamma^{(3)}$. To be specific, the topological character of the C_3 -symmetric hexagonal unit cell is given by

$$\bar{\chi}^{(3)} = (\#\Gamma^{(3)}, \#K_2^{(3)}, \#K_3^{(3)}) \quad (A2)$$

Considering Eq. (A2), the modified fractional corner charge invariants and the symmetry behaviors are listed in Table A1 for some possible cases.

In Table A1, the red colored invariants $Q_q^{(3)}$ are modified from Eq. (A2). This modification is derived from the fact that the degenerate states in $\#\Gamma^{(3)}$ always appear in a pair; or not, it is gapless (Ma and Shvets, 2016, Wu and Hu, 2015, Košata and Zilberberg, 2021, Xu et al., 2016, Zhang et al., 2017). For the unpaired case, it is ambiguous to be tagged as $\Gamma_2^{(3)}$ or $\Gamma_3^{(3)}$, hence the invariants $Q_q^{(3)}$ in the last four cases cannot be solely identified by the $\bar{\chi}^{(3)}$ in Eq. (A2). Therefore, when $\#\Gamma^{(3)}$ is odd, the corresponding fractional corner charge should be modified into zero with gapless band reality. When $\#\Gamma^{(3)}$ is even, number $\#\Gamma^{(3)}$ can be equivalently divided as: $\#\Gamma_2^{(3)} = \#\Gamma_3^{(3)} = \#\Gamma^{(3)}/2$.

Thus, the modified fractional corner charge invariant gives

$$Q^{(3)} = \left(\frac{1}{3} \left(\#K_{q \neq 1}^{(3)} - \frac{1}{2} \#\Gamma^{(3)} \right) \bmod 1 \right) \times ((\#\Gamma^{(3)} + 1) \bmod 2) \quad (A3)$$

where the red terms aim to avoid the unpaired two-order degenerate states.

Appendix B: Modification of the pseudo-spin invariant

Especially for the C_3 - or C_6 -symmetric hexagonal unit cells with the TRS, we trace the broken (double) Dirac cones at the K or Γ points, and give out their topological characters (Košata and Zilberberg, 2021, Schindler et al., 2019)

$$\bar{\chi}^{(3)} = (\#K_2^{(3)}, \#K_3^{(3)}) \bar{\chi}^{(6)} = (\#\Gamma_1^{(2)}, \#\Gamma_2^{(2)}, \#\Gamma^{(3)}) \quad (B1)$$

Here, $\#\Gamma^{(3)}$ counts the two-order degenerate states of the Γ point in the C_3 operator. The modified pseudo-spin invariants and their symmetry behaviors are listed in Table B1 and Table B2 for some possible cases.

Different as scaling a function (Christensen et al., 2022, Watanabe and Lu, 2018), the operation of a symmetry operator \hat{g} on a vector function $f(r)$ transforms as $\hat{g}f(r) = \hat{R}f(\hat{g}^{-1}r)$, where \hat{R} is the rotational operator in \hat{g} . For the present symmetry groups (C_3 or C_6) in our paper, all group elements behave as a rotation around z -axis, and the transformation can be simplified as $\hat{g}U(r) = \hat{R}U_T(\hat{g}^{-1}r) + \hat{R}U_L(\hat{g}^{-1}r)$, where $U = U_T + U_L = (u, v, 0)^\top + (0, 0, w)^\top$ is the displacement vector in mechanics. This decomposed equation implies the symmetry of state can be determined by either U_T or U_L , except for the singular cases with displacement component $U_T = \mathbf{0}$ or $U_L = \mathbf{0}$. For simplicity, we determine the symmetry indicators only using w .

In the original SI theory (Schindler et al., 2019, Benalcazar et al., 2019), the counted bands should be isolated from others. And an alternative approach is to count all bands below the target band gap in the photonic and phononic systems. However, the first three bands always converge to plane waves when $|k| \rightarrow 0$, where two translational motions produce two singularities with $U_L = \mathbf{0}$ (Christensen et al., 2022, Watanabe and Lu, 2018). In Table B2, the red-colored data reveal the symmetry behaviors of the first three bands that always cross through the singularities around the zero energy. Hence, we defined the modified pseudo-spin invariants to over-count those singularities as

$$\begin{aligned} Z^{(3)} &= \text{sgn}(\#K_2^{(3)} - \#K_3^{(3)}) \\ Z^{(6)} &= \text{sgn}(\#\Gamma_p^{(6)} - \#\Gamma_d^{(6)} \text{rgb}) [1, 0, 0 - \text{rgb}] [1, 0, 02] \end{aligned} \quad (B2)$$

where the terms $\#\Gamma_p^{(6)}$ and $\#\Gamma_d^{(6)}$ count the p and d states at the Γ point, and the red term is the modification from the singularities,

Table B1

The symmetry behaviors of the C_3 -symmetric unit cells with TRS (for the pseudo-spin invariants).

Z ⁽³⁾	#K ₂ ⁽³⁾	#K ₃ ⁽³⁾
1	1	0
1	2	0
-1	0	1
0	1	1

Table B2

The symmetry behaviors of the C_6 -symmetric unit cells with TRS (for the pseudo-spin invariants).

$Z^{(6)}$	$\#\Gamma_1^{(2)}$	$\#\Gamma_2^{(2)}$	$\#\Gamma^{(3)}$	state
-1	2	0	2	2d
1	0	2	2	2p
0	2	2	4	2p + 2d
0	1	0	0	1s
0	0	1	0	1f
0	1	2	2	1s+2p

which should be marked as p states. For the case of photonics, the Eq. (B2) should be further modified as the work (Christensen et al., 2022).

Appendix C: The setup of the optimization and the GA solver

For the parameters of material and optimization solver in our paper, the setup gives: the basic medium is epoxy (EP)¹ with Young's modulus $E_0 = 4.35\text{GPa}$, the Poisson's ratio $\nu_0 = 0.37$, and the mass density $\rho_0 = 1180\text{kg} \cdot \text{m}^{-3}$. The scattering medium is steel (Fe) with Young's modulus $E = 200\text{GPa}$, the Poisson's ratio $\nu = 0.2$, and the mass density $\rho = 7800\text{kg} \cdot \text{m}^{-3}$. The genetic algorithm (GA) solver is set as: the population size of 100, the crossover fraction of 0.9, the migration fraction of 0.3, the elite size of 5, the objec-tivation tolerance of 1e-5, the stall generation limit of 15. The lattice constant is $A = |\mathbf{R}| = 1\text{m}$. The supercell is constructed through a horizontal work plane at the middle of all unit cells.

Table C1 and Fig. C1 list some typical optimized unit cells. The row number in Table C1 is consistent with the order of unit cells in Fig. C1. For the examples in the main text, we set their optimization procedure as

- For the C_3 -symmetric (valley-based) helical MTIs, the broken Dirac cone appears at the K point. The first unit cell is optimized with setting $m = 6$, nonzero topological invariants (2/3, 1) and no specific f_{ref} , which will auto-update as the mid-frequency of the target gap.

Table C1

Some typical optimized unit cells for the C_3 - and the -symmetric TMs. (Here, the red data refers to the examples presented in our paper).

C_n	$\mathbf{r}\{A\}$	$\mathbf{L}\{A\}$	$\Phi\{\text{deg}\}$	$H\{A\} (Q^{(n)}, Z^{(n)})$	$f_{\max}^{(m)} \sim f_{\min}^{(m+1)}$
C_3	(0.7217, 0.95, 0.0275) (0.3382, 0.5073, 0.1691)	(108, 18, 126)	0.55	(2/3, 1)	0.741~1.069
	(0.4041, 1.00, 0.0900) (0.3082, 0.3082, 0.2568)	(144, 72, 90)	0.45	(2/3, -1)	0.772~1.000
C_6	(0.9238, 0.90, 0.3250) (0.3682, 0.2455, 0.3068)	(90, 108, 0)	0.65	(1/2, 1)	1.344~1.489
	(0.8776, 0.90, 0.1750) (0.2155, 0.3232, 0.2693)	(90, 144, 72)	0.50	(0, -1)	1.332~1.450
	(0.9584, 0.80, 0.1800) (0.1766, 0.4121, 0.2355)	(126, 126, 72)	0.60	(1/2, 1)	1.254~1.319
	(0.8603, 0.95, 0.1575) (0.2055, 0.3596, 0.3082)	(108, 144, 90)	0.45	(0, -1)	1.249~1.344

¹ It is worth noting that, the damping of Epoxy may significantly affect the transmission efficiency of the topological propagation of elastic wave in practice. Since the present work focuses on developing a topology optimization paradigm for three-dimensional mechanical higher-order topological insulators and the design method has no restriction on the choice of base materials, we evaluate the optimized designs without considering the damping effect of Epoxy. Furthermore, mechanical topological insulators made of Fe and Air, in which the damping effect is negligible, are obtained by the proposed design approach in Appendix F.

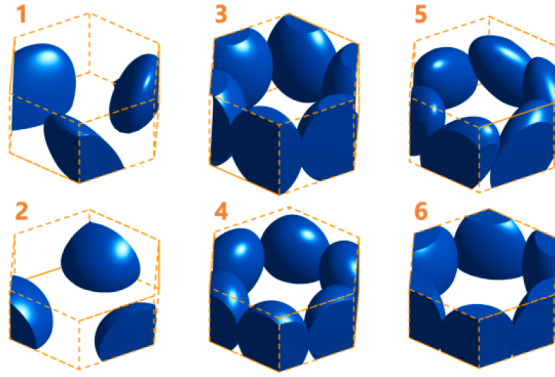


Fig. C1. Some optimized unit cells with the C_3 and C_6 symmetries. The order refers to the row number of Table C1.

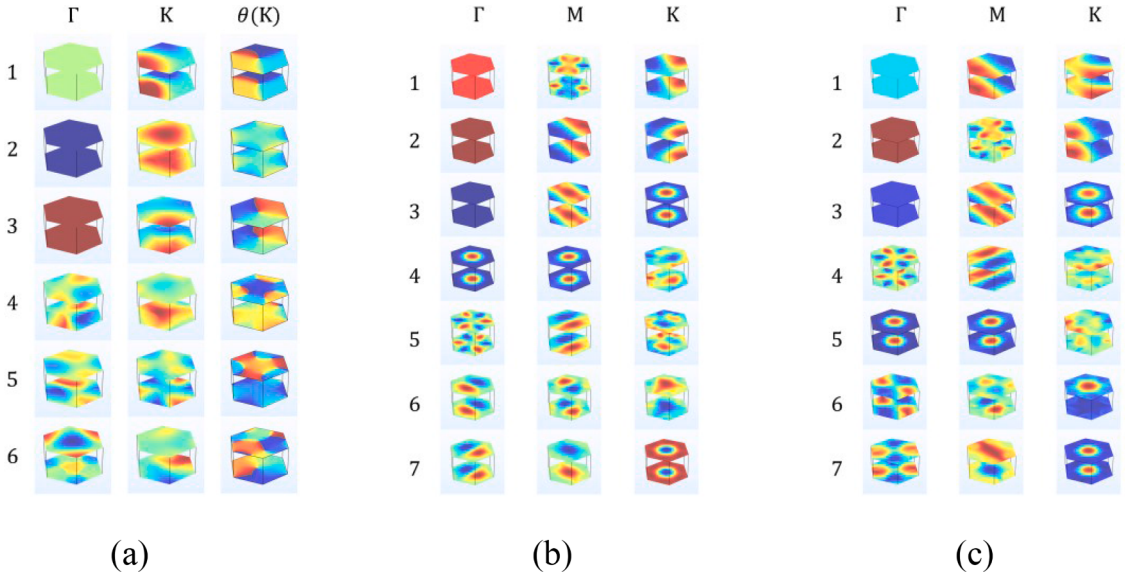


Fig. C2. The states at high-symmetry points of the optimized TMs. (a) The $\mathcal{R}_e(w)$ and $\theta(w)$ fields of the 1st C_3 -symmetric unit cell in Table C1. (b) and (c) The $\mathcal{R}_e(w)$ fields of the 1st and 2nd C_6 -symmetric unit cell in Table C1, respectively.

- For the C_6 -symmetric (spin-based) helical MTIs, the broken Dirac cone appears at the Γ point. The first unit cell is optimized with setting $m = 7$, $(Q_{\text{ref}}^{(n)}, Z_{\text{ref}}^{(n)}) = (1/2, 1)$, and $f_{\text{ref}} = 1.4$. Then the MTI partner is optimized with setting $m = 7$, $(Q_{\text{ref}}^{(n)}, Z_{\text{ref}}^{(n)}) = (0, -1)$, and $f_{\text{ref}} = 1.4$.

For the visualization of the SIs in Fig. 5 and Fig. 7, the states of the high-symmetry points are shown in Fig. C2. It is determined that (1) for the C_3 -symmetric helical MTIs, the counts are $\#\Gamma^{(3)} = 4$, $\#K_2^{(3)} = 2$ and $\#K_3^{(3)} = 1$, so we set $\#K_{q \neq 1}^{(3)} = 1$ to obtain a nonzero $Q^{(3)}$ in Eq. (8); (2) for the 1st C_6 -symmetric helical MTIs, $[M_1^{(2)}] = 4 - 2 = 2$, $[K_1^{(3)}] = 3 - 3 = 0$, $\#\Gamma_p^{(6)} = 4$ ($\Gamma_p^{(6)}$ requires $\Gamma_q^{(6)} = \xi$ and $\Gamma_q^{(2)} = -1$) and $\#\Gamma_d^{(6)} = 0$ ($\Gamma_d^{(6)}$ requires $\Gamma_q^{(3)} = \xi$ and $\Gamma_q^{(2)} = +1$); (3) for the 2nd C_6 -symmetric helical MTIs, $[M_1^{(2)}] = 4 - 4 = 0$, $[K_1^{(3)}] = 3 - 3 = 0$, $\#\Gamma_p^{(6)} = 2$ and $\#\Gamma_d^{(6)} = 2$. The combination of states with $K_2^{(3)}$ and $K_3^{(3)}$ form the paired degenerate states in the C_3 -symmetric unit cells, and there is one unpaired degenerate state left in the case (1). For the C_6 -symmetric unit cells, the count difference between $\#\Gamma_p^{(6)}$ and $\#\Gamma_d^{(6)}$ shows 4 unpaired degenerate states in the case (2), while no unpaired degenerate state in the case (3).

To illustrate the effectiveness of the proposed design framework, the statistical charts in Fig. 4(b) present a catalogue for various unit cells. To be specific, 1) for the case with invariants $(0, Z^{(n)} \neq 0)$, all C_3 -symmetric unit cells belong to the QVTIs and the C_6 -symmetric unit cells belong to the QSTIs; 2) for the case with invariants $(Q^{(n)} \neq 0, 0)$, all unit cells are the MTIs; 3) for the case with invariants $(Q^{(n)} \neq 0, Z^{(n)} \neq 0)$, all C_3 - and C_6 -symmetric unit cells are the helical MTIs; 4) for the case with invariants $(0, 0)$, these materials are the trivial insulators.

Appendix D: The supercell's setup for the edge and the corner states

The setups for supercells are detailed as

- For the C_3 -symmetric unit cells in the main text, the script of the truncated supercell is shown in Fig. D1, where it provides an approach to adjust the frequency of the edge states. This truncation does not break the crystalline symmetry, and the topological edge states would not vanish. In Fig. D1(a) and (b), the truncation is set as $T = 1/4 \times 2A/\sqrt{3}$, and the edge gap is between 0.872–1.001. In Fig. D1(c) and (d), the eigenvalue spectrum and the crossing waveguide are simulated with the truncation $T = 1 \times 2A/\sqrt{3}$. The light-blue areas in Fig. D1 refer to the supercell's structures in the main text.

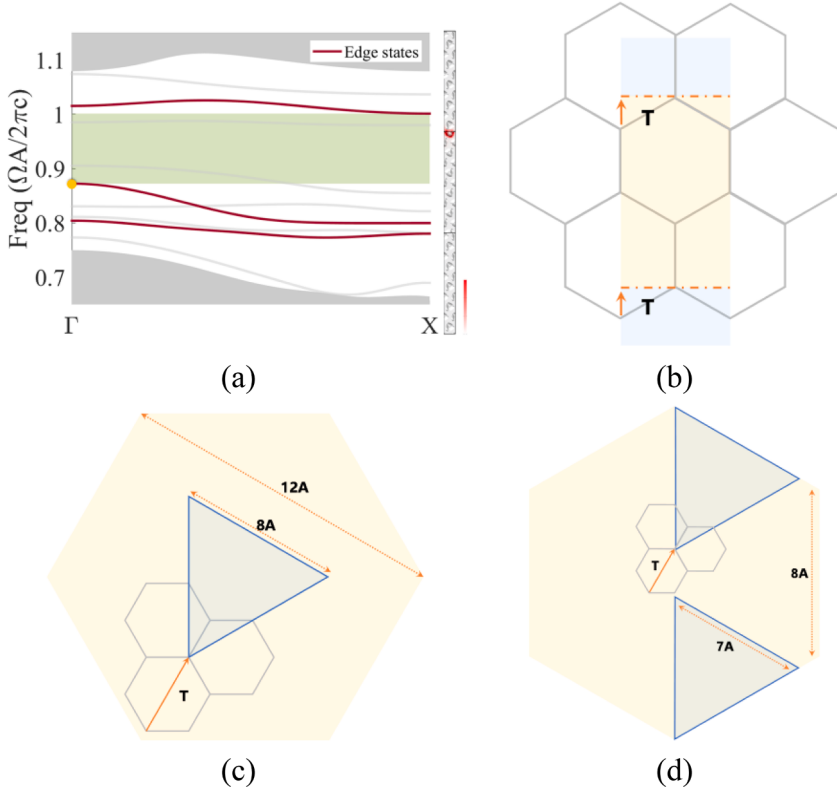


Fig. D1. The supercell's scripts of the C_3 -symmetric unit cell. (a) The band of the edge state (light-grey band belongs to the lower interface counterpart). (b) The script of the ribbon-shaped supercell in (a). The supercell's script (c) for the eigenvalue spectrum and (d) for the simulation in the crossing waveguide.

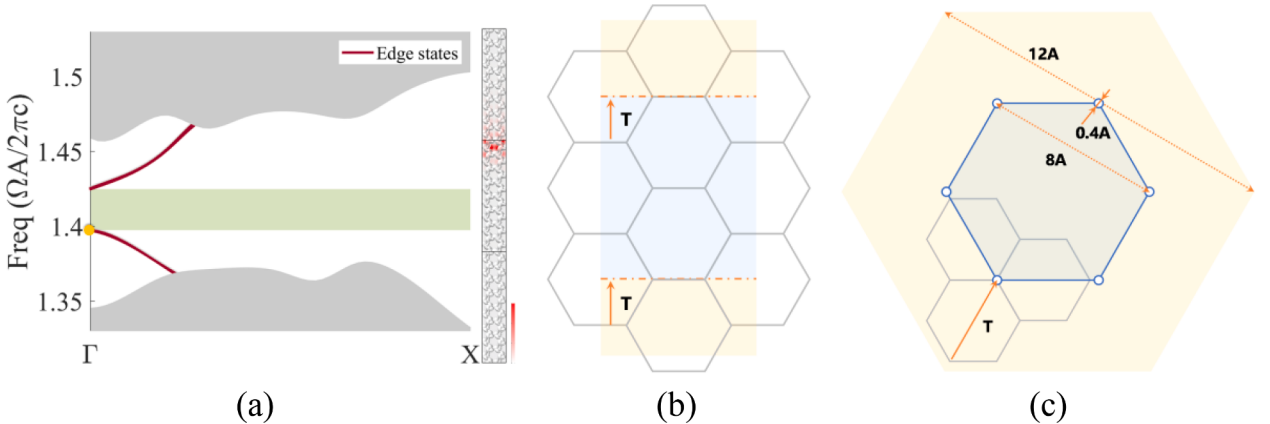


Fig. D2. The supercell's scripts for the C_6 -symmetric unit cell. (a) The band of the edge states. (b) The script of the ribbon-shaped supercell in (a). (c) The supercell's script for the eigenvalue spectrum.

- For the C_6 -symmetric unit cells, the inner interface between the unit cell pairs can be alternatively truncated as Fig. D2. In Fig. D2 (a) and (b), the gap of the edge states is found between 1.398-1.425 with the truncation $T = 1/2 \times A$. The supercell's script for the eigenvalue spectrum is displayed in Fig. D2(c) with the truncation $T = 1 \times 2A/\sqrt{3}$. In Fig. D2(c), except for the inner hexagonal interface, six base medium cylinders with a diameter of $0.4A$ are added to adjust the supercell's corners. The light-blue areas in Fig. D2 refer to the supercell's structures in the main text.

Appendix E: Effect of the component's number on the optimized MTIs

For the C_3 -symmetric unit cells, two components identifying the Fe phase are optimized in the reduced design domain as well. At this circumstance, the number of design variables would be 19, and a larger design space is explored. Within 50 generations, the design variables converge to $D = (0.8949, 0.95, 0.045, 0.3082, 0.4109, 0.3082, 72, 126, 162, 0.8372, 0.75, 0.09, 0.1541, 0.1541, 0.1541, 18, 54, 72, 0.45)^\top$. As expected, for the latter case, on the one hand, a smaller objective function value (-0.172 vs -0.155) as well as a larger normalized width of band gap (0.358 vs 0.328) are achieved; on the other hand, more generations are required in the optimization process (as shown in Fig. E1), while the geometry is more complex and would bring more challenges for fabrication.

Since it is focused on developing a rational design paradigm for MTIs, rather than perusing the MTIs with global optimality, we adopt 1 component in each reduced design domain of the unit cell in the present work.

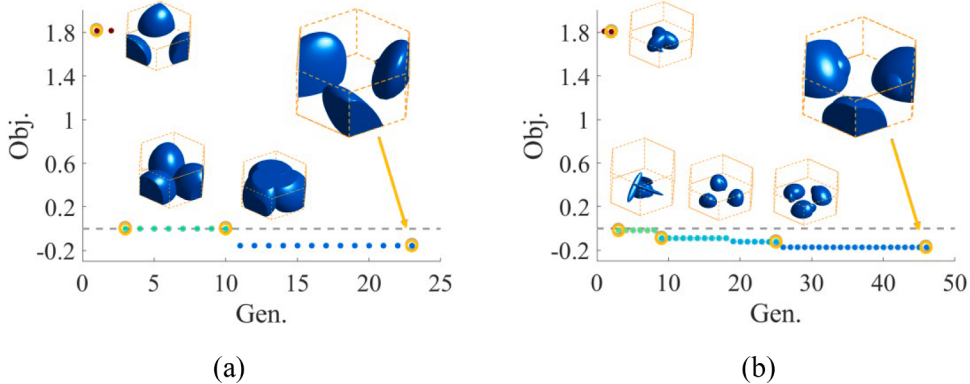


Fig. E1. The convergence history of the optimized C_3 -symmetric unit cells (a) with 1 component and (b) with 2 components in the reduced design domain, respectively.

Appendix F: Optimal designs of the Fe-Air based mechanical TMs

To illustrate the generality of this optimization framework, we designed some mechanical TMs, made of the Fe-Air medium as well. Fig. F1 and Table F1 show some available optimal designs.

For the optimized C_3 -symmetric unit cell in Fig. F1(a)-(c) and UC1 in Fig. F1(d), its invariant is $(1/3, 1)$ and the range of concerned band gap is 0.620-0.703. We also present the symmetry-behavior-table and profiles of the states at the high symmetry points. According to the classification rule in Appendix C, this is a helical MTI.

For the optimized C_6 -symmetric unit cell in Fig. F1(e)-(g) and UC4 in Fig. F1(h), its invariant is $(0, 1)$ and the range of concerned band gap is 0.708-0.826. This is a QSTI. Notably, the flat bands in the band structure implies a strong local vibration. This unit cell is called the perturbative metamaterials (Matlack et al., 2018), in which the weak interaction allows us to associate it with the discrete model. This example further demonstrates the effectiveness of our optimization framework for designing 3D topological materials.

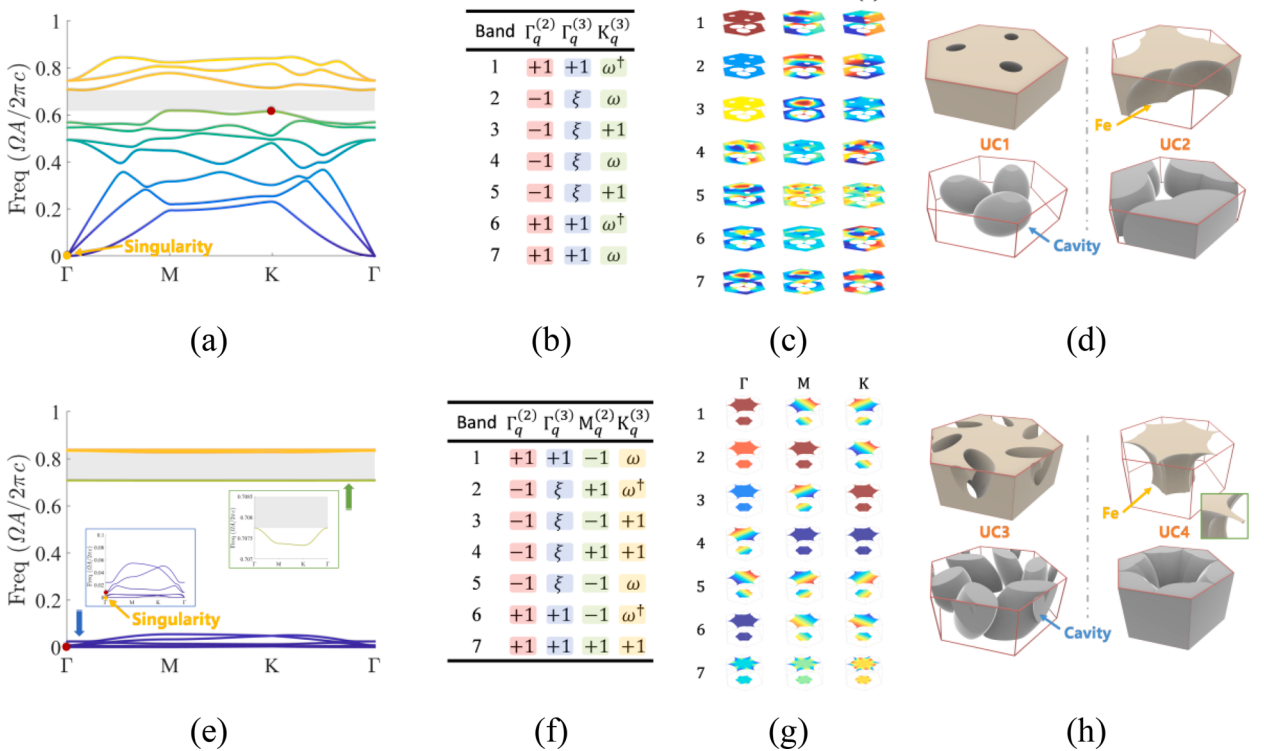


Fig. F1. The optimized C_3 -symmetric and C_6 -symmetric mechanical TMs composed of Fe and Air. (a) and (e) The band structure with the unpaired states and singularity states identified by the red and yellow points, respectively. (b) and (f) The symmetry-behavior-tables. (c) and (g) The $\theta(w)$ and $\phi(w)$ fields for states at the high-symmetry points. (d) and (h) Some available optimal designs. The information of design variables, topological invariants and band gap are listed in Table F1 with the same order. Especially, more information about the unit cells of (a)-(c) and (e)-(g) is highlighted in red in Table F1, respectively.

Table F1

Some typical optimized unit cells for the C_3 - and the C_6 -symmetric TMs. (Here, the red data refers to the examples presented in Fig. F1).

C_n	$r\{A\}$	$L\{A\}$	$\Phi\{\text{deg}\}$	$H\{A\}$	$(Q^{(n)}, Z^{(n)})$	$f_{\max}^{(m)} \sim f_{\min}^{(m+1)}$
C_3	(0.4619, 0.7, 0.1050)	(0.1755, 0.1755, 0.2632)	(54, 162, 180)	0.30	(1/3, 1)	0.620~0.703
	(1.0392, 0.6, 0.1125)	(0.3082, 0.3596, 0.4109)	(144, 126, 108)	0.4	(1/3, -1)	0.658~0.703
C_6	(0.9122, 0.6, 0.2000)	(0.1955, 0.0977, 0.3909)	(216, 90, 198)	0.4	(1/2, 1)	0.419~0.447
	(0.8762, 0.95, 0.1650)	(0.3946, 0.3382, 0.4791)	(180, 72, 306)	0.55	(0, 1)	0.708~0.826

References

- Achenbach, J.D., 1973. Wave Propagation in Elastic Solids. Elsevier Science Publishing Co Inc.
- Bandres, M.A., et al., 2018. Topological insulator laser: experiments. *Science* (1979) 359, eaar4005.
- Benalcazar, W.A., Bernevig, B.A., Hughes, T.L., 2017. Quantized electric multipole insulators. *Science* (1979) 357, 61–66.
- Benalcazar, W.A., Li, T., Hughes, T.L., 2019. Quantization of fractional corner charge in C_n -symmetric higher-order topological crystalline insulators. *Phys. Rev. B* 99, 245151.
- Bendsoe, M.P., Sigmund, O., 2004. Topology Optimization: Theory, Methods, and Applications. Springer Berlin Heidelberg.
- Bradlyn, B., et al., 2017. Topological quantum chemistry. *Nature* 547, 298–305.
- Bradlyn, B., et al., 2018. Band connectivity for topological quantum chemistry: Band structures as a graph theory problem. *Phys. Rev. B* 97, 035138.
- Chen, Y., Liu, X., Hu, G., 2019. Topological phase transition in mechanical honeycomb lattice. *J. Mech. Phys. Solids* 122, 54–68.
- Chen, Y., Meng, F., Kivshar, Y., Jia, B., Huang, X., 2020. Inverse design of higher-order photonic topological insulators. *Phys. Rev. Res.* 2, 23115.
- Christensen, T., Po, H.C., Joannopoulos, J.D., Soljačić, M., 2022. Location and topology of the fundamental gap in photonic crystals. *Phys. Rev. X* 12, 21066.
- Christiansen, R.E., Wang, F., Sigmund, O., Stobbe, S., 2019. Designing photonic topological insulators with quantum-spin-Hall edge states using topology optimization. *Nanophotonics* 8, 1363–1369.
- Dong, H.W., et al., 2021. Customizing acoustic Dirac cones and topological insulators in square lattices by topology optimization. *J. Sound Vib.* 493, 115687.

- Du, Z., Chen, H., Huang, G., 2020. Optimal quantum valley Hall insulators by rationally engineering Berry curvature and band structure. *J. Mech. Phys. Solids* 135, 103784.
- Du, Z., et al., 2022. An efficient and easy-to-extend Matlab code of the moving morphable component (MMC) method for three-dimensional topology optimization. *Struct. Multidiscip. Optim.* 65, 158.
- Fan, H., Xia, B., Tong, L., Zheng, S., Yu, D., 2019. Elastic higher-order topological insulator with topologically protected corner states. *Phys. Rev. Lett.* 122, 204301.
- Fu, L., Kane, C.L., 2007. Topological insulators with inversion symmetry. *Phys. Rev. B* 76, 45302.
- Ghasemi, H., Park, H.S., Rabczuk, T., 2018. A multi-material level set-based topology optimization of flexoelectric composites. *Comput. Methods Appl. Mech. Eng.* 332, 47–62.
- Gong, Y., Wong, S., Bennett, A.J., Huffaker, D.L., Oh, S.S., 2020. Topological insulator laser using valley-Hall photonic crystals. *ACS Photon.* 7, 2089–2097.
- Guo, X., Zhang, W., Zhong, W., 2014. Doing topology optimization explicitly and geometrically—a new moving morphable components based framework. *J. Appl. Mech.* 81, 81009.
- Hafezi, M., Demler, E.A., Lukin, M.D., Taylor, J.M., 2011. Robust optical delay lines with topological protection. *Nat. Phys.* 7, 907–912.
- Hasan, M.Z., Kane, C.L., 2010. Colloquium : topological insulators. *Rev. Mod. Phys.* 82, 3045.
- Hoffmann, R., 1987. How chemistry and physics meet in the solid state. *Angew. Chem. Int. Ed Engl.* 26, 846–878.
- Kang, Y., Ni, X., Cheng, X., Khanikaev, A.B., Genack, A.Z., 2018. Pseudo-spin-valley coupled edge states in a photonic topological insulator. *Nat. Commun.* 9, 3029.
- Kim, M., Jacob, Z., Rho, J., 2020. Recent advances in 2D, 3D and higher-order topological photonics. *Light Sci. Appl.* 9, 130.
- Kosata, J., Zilberberg, O., 2021. Second-order topological modes in two-dimensional continuous media. *Phys. Rev. Res.* 3, L032029.
- Kreisselmeier, G., Steinhauser, R., 1980. Systematic control design by optimizing a vector performance index. *Comput. Aided Des. Contr. Syst.* 113–117.
- Kumar, A., et al., 2022. Topological sensor on a silicon chip. *Appl. Phys. Lett.* 121, 11101.
- Liu, F., Deng, H.Y., Wakabayashi, K., 2019. Helical topological edge states in a quadrupole phase. *Phys. Rev. Lett.* 122, 86804.
- Long, Y., Ren, J., Chen, H., 2018. Intrinsic spin of elastic waves. *Proc. Natl. Acad. Sci.* 115, 9951–9955.
- Lu, Y., Park, H.S., 2021. Double Dirac cones and topologically nontrivial phonons for continuous square symmetric C4(v) and C2(v) unit cells. *Phys. Rev. B* 103, 64308.
- Lu, L., Joannopoulos, J.D., Soljačić, M., 2014. Topological photonics. *Nat. Photon.* 8, 821–829.
- Luo, J., et al., 2021a. Moving morphable components-based inverse design formulation for quantum valley/spin Hall insulators. *Extreme Mech. Lett.* 45, 101276.
- Luo, J., et al., 2021b. Multi-class, multi-functional design of photonic topological insulators by rational symmetry-indicators engineering. *Nanophotonics* 10, 4523–4531.
- Ma, T.X., Fan, Q.S., Zhang, C., Wang, Y.S., 2022. Flexural wave energy harvesting by the topological interface state of a phononic crystal beam. *Extreme Mech. Lett.* 50, 101578.
- Ma, T., Shvets, G., 2016. All-Si valley-Hall photonic topological insulator. *New J. Phys.* 18, 025012.
- Matlack, K.H., Serra-Garcia, M., Palermo, A., Huber, S.D., Daraio, C., 2018. Designing perturbative metamaterials from discrete models. *Nat. Mater.* 17, 323–328.
- Mousavi, S.H., Khanikaev, A.B., Wang, Z., 2015. Topologically protected elastic waves in phononic metamaterials. *Nat. Commun.* 6, 8682.
- Nanthakumar, S.S., et al., 2019. Inverse design of quantum spin Hall-based phononic topological insulators. *J. Mech. Phys. Solids* 125, 550–571.
- Nii, Y., Onose, Y., 2023. Imaging an acoustic topological edge mode on a patterned substrate with microwave impedance microscopy. *Phys. Rev. Appl.* 19, 014001.
- Peano, V., Sapper, F., Marquardt, F., 2021. Rapid exploration of topological band structures using deep learning. *Phys. Rev. X* 11, 21052.
- Po, H.C., Vishwanath, A., Watanabe, H., 2017. Symmetry-based indicators of band topology in the 230 space groups. *Nat. Commun.* 8, 50.
- Po, H.C., Vishwanath, A., Watanabe, H., 2017. Complete theory of symmetry-based indicators of band topology. *Nat. Commun.* 8, 50.
- Süsstrunk, R., Huber, S.D., 2015. Observation of phononic helical edge states in a mechanical topological insulator. *Science (1979)* 349, 47–50.
- Schindler, F., et al., 2019. Fractional corner charges in spin-orbit coupled crystals. *Phys. Rev. Res.* 1, 33074.
- Strang, G., 1993. Introduction to Linear Algebra. Wellesley Cambridge Press.
- Tang, F., Po, H.C., Vishwanath, A., Wan, X., 2019. Topological materials discovery by large-order symmetry indicators. *Sci. Adv.* 5, eaau8725.
- Watanabe, H., Lu, L., 2018. Space group theory of photonic bands. *Phys. Rev. Lett.* 121, 263903.
- Watanabe, H., Po, H.C., Vishwanath, A., 2018. Structure and topology of band structures in the 1651 magnetic space groups. *Sci. Adv.* 4, eaat8685.
- Wu, L.H., Hu, X., 2015. Scheme for achieving a topological photonic crystal by using dielectric material. *Phys. Rev. Lett.* 114, 223901.
- Wu, Q., Chen, H., Li, X., Huang, G., 2020. In-plane second-order topologically protected states in elastic Kagome lattices. *Phys. Rev. Appl.* 14, 014084.
- Xie, B., et al., 2021. Higher-order band topology. *Nat. Rev. Phys.* 3, 520–532.
- Xu, L., Wang, H.-X., Xu, Y.-D., Chen, H.-Y., Jiang, J.-H., 2016. Accidental degeneracy in photonic bands and topological phase transitions in two-dimensional core-shell dielectric photonic crystals. *Opt. Express* 24, 18059.
- Xu, Y., et al., 2022. Catalogue of topological phonon materials. ArXiv.
- Yang, Z.Z., Li, X., Peng, Y.Y., Zou, X.Y., Cheng, J.C., 2020. Helical higher-order topological states in an acoustic crystalline insulator. *Phys. Rev. Lett.* 125, 255502.
- Yu, S.Y., et al., 2018. Elastic pseudospin transport for integrable topological phononic circuits. *Nat. Commun.* 9, 3072.
- Zhang, Z., et al., 2017. Topological creation of acoustic pseudospin multipoles in a flow-free symmetry-broken metamaterial lattice. *Phys. Rev. Lett.* 118, 84303.
- Zhang, Z., et al., 2018. Directional acoustic antennas based on valley-Hall topological insulators. *Adv. Mater.* 30, 1803229.
- Zhang, Z., et al., 2018. Topological acoustic delay line. *Phys. Rev. Appl.* 9, 34032.
- Zhang, Z., et al., 2019. Deep-subwavelength holey acoustic second-order topological insulators. *Adv. Mater.* 31, 1904682.
- Zhang, X., et al., 2019. Second-order topology and multidimensional topological transitions in sonic crystals. *Nat. Phys.* 15, 582–588.
- Zhou, W., et al., 2020. Actively controllable topological phase transition in homogeneous piezoelectric rod system. *J. Mech. Phys. Solids* 137, 103824.
- Zhu, X., et al., 2018. Topological transitions in continuously deformed photonic crystals. *Phys. Rev. B* 97, 85148.